

Supporting Information

## Texturing In-Situ: N, S-Enriched Hierarchically Porous Carbon as Highly Active Reversible Oxygen Electrocatalysts

Zengxia Pei,<sup>a</sup> Hongfei Li,<sup>a</sup> Yan Huang,<sup>a</sup> Qi Xue,<sup>a</sup> Yang Huang,<sup>b</sup> Minshen Zhu,<sup>a</sup> Zifeng Wang<sup>a</sup> and Chunyi Zhi<sup>a,c\*</sup>

<sup>a</sup>Department of Physics and Materials Science, City University of Hong Kong, Hong Kong, China.

<sup>b</sup>College of Materials Science and Engineering, Shenzhen University, Shenzhen 518000, China.

<sup>c</sup>Shenzhen Research Institute, City University of Hong Kong, Shenzhen 518000, China.

\*e-mail: cy.zhi@cityu.edu.hk

### Experimental Section

**Materials Synthesis.** The macro-porous N, S-doped carbon (CNS) was synthesized using as a hard template method. Typically, 1 g silica powder (fumed, particle size *ca.* 0.2-0.3  $\mu\text{m}$ , Sigma-Aldrich) was dispersed into 30 mL DI water, followed by addition of 1 g sucrose, 1 g trithiocyanuric acid (TA) and 0.1 g sulfuric acid (96-97 wt%). This mixture solution was then sonicated for 10 min being heated up to 100  $^{\circ}\text{C}$  for liquid evaporation. The remaining solid was then kept at 160  $^{\circ}\text{C}$  for 10 hrs to polymerize the sucrose and cross-link the TA monomers. The weight percent of the  $\text{SiO}_2$  within the mixture was determined by TGA. A certain amount of the obtained powder was then finely grinded and mixed uniformly with an excess amount of Teflon powder (5  $\mu\text{m}$ ) ( $\text{SiO}_2$ : Teflon= 1:12, weight ratio), which was subject to calcination at 600  $^{\circ}\text{C}$  for 1 h and further calcined at different eventual temperatures (800-1100  $^{\circ}\text{C}$ ) for 3 hrs under Ar atmosphere with an identical ramp rate of 5  $^{\circ}\text{C min}^{-1}$ . The resulted powder can be readily used as catalyst directly. The samples are named as T-CNS, where T stands for the pyrolysis temperatures (800-1100  $^{\circ}\text{C}$ ).

**Physicochemical Characterization.** The crystal structure of the catalyst was identified by a Bruker D2 Phaser X-ray diffractometer with Cu  $K_{\alpha}$  radiation ( $\lambda =$

0.15418 nm) operating at 30 kV and 10 mA, respectively. Raman scattering measurements were performed with a multichannel modular triple Raman system (Renishaw Co.) with confocal microscopy at room temperature using the 633 nm laser. The morphology and microstructure of the samples were revealed by a JEOL-2001F field-emission TEM, and the accessory EELS was used to determine to composite elements. XPS analyses were conducted on an ESCALAB 250 photoelectron spectroscopy (Thermo Fisher Scientific) at  $1.2 \times 10^{-9}$  mbar using Al  $K_{\alpha}$  X-ray beam (1486.6 eV). The XPS spectra were charge corrected to the adventitious C 1s peak at 284.5 eV. TGA were carried out on a TA #SDT Q600 analyser at 30-800 °C with an O<sub>2</sub> flow of 40 mL min<sup>-1</sup>. The nitrogen adsorption and desorption isotherms were characterized using a Micrometrics ASAP 2020 analyzer. Pore size distribution and specific surface area were obtained via Barrett-Joyner-Halenda (BJH) and Brunauer-Emmett-Teller (BET) methods from adsorption branch of the isotherm, at a relative pressure range of  $P/P_0 = 0.06-0.25$ .

**Electrochemical Measurements.** All electrochemical measurements were carried out on a CHI 760D electrochemical workstation integrated with a RRDE-3A rotating ring disk electrode apparatus in a typical 3-electrode system, in which a glassy carbon electrode (GCE, 3mm in diameter) loaded with different catalysts was used as working electrode, with a Ag/AgCl (in 3 M KCl) electrode and a Pt mesh as reference and counter electrode, respectively. The recorded potential was converted to a reversible hydrogen electrode (RHE). 0.1 M KOH or 0.1 M HClO<sub>4</sub> solution served as the electrolyte for ORR measurements. The loading masses for metal-free catalysts were 140 μg cm<sup>-2</sup> for alkaline solution and 600 μg cm<sup>-2</sup> for acidic electrolyte. Pt/C (Alfa Acesar, 20 wt%) with a loading mass of 140 μg cm<sup>-2</sup> was used for reference. The onset potential ( $E_{\text{onset}}$ ) for ORR is defined as the critical potential where the reduction current density reaches 1% of the limiting current density. All the ORR currents presented in the figures are Faradaic currents, i.e., after correction for the capacitive current. Each catalyst was repeated at least 3 times for the above measurements to exclude possible incidental errors.

The RRDE tests were conducted with a Pt ring surrounded 4 mm diameter GCE. The Pt ring electrode was set at 1.5 V (vs. RHE) to detect the generated HO<sub>2</sub><sup>-</sup> species. The value of n was also calculated through RRDE tests:

$$n = \frac{4i_d}{i_d + \frac{i_r}{N}}$$

the HO<sub>2</sub><sup>-</sup> yield was calculated from equation:

$$HO_2^- \% = \frac{200i_r}{N(i_d + \frac{i_r}{N})}$$

here  $i_d$  and  $i_r$  are the disk current and ring current, respectively, and  $N$  is the current collection efficiency of the Pt ring and was determined to be 0.37.

Long term stability tests in ORR were conducted by measuring the current changes of the catalyst modified GCE at a fixed potential of 0.7 V (vs. RHE) and a rotation speed of 1600 rpm in O<sub>2</sub> saturated electrolyte. The cross-over tolerance tests were performed by comparing the CV curves before and after the addition of 10 vol% methanol into the electrolyte.

For OER measurements, the electrolyte was O<sub>2</sub> saturated 0.1 or 1 M KOH solution and the catalyst loading mass was 420  $\mu\text{g cm}^{-2}$  for metal-free sample and 140  $\mu\text{g cm}^{-2}$  for noble-metal materials (Pt/C and IrO<sub>2</sub>). The LSV curves were obtained at a scan rate of 5 mV s<sup>-1</sup> and the GCE was rotated at 1600 rpm to alleviate the accumulation of evolved oxygen bubbles on the electrode surface. All the OER currents presented in the figures are Faradaic currents, i.e., after correction for the capacitive current. The  $E_{\text{onset}}$  for OER is defined as the critical potential where the current density reaches 0.5 mA cm<sup>-2</sup>. All the curves were iR corrected unless otherwise stated and in order to get a stable current, the LSV data were collected at the second sweep.

**Zn-air battery assembly.** The air electrodes for Zn-air battery use stainless steel mesh (SSM) as backing layer, with a gas diffusion layer (GDL) on the air-facing side and catalyst on the water-facing side. A carbon ink consists of carbon black and polytetrafluoroethylene (PTFE) emulsion (60 wt%) according to a mass of 3:7 was painted onto the backing layer to form the GDL, which then subject to heating at 200 °C for 30 min. The catalyst was then loaded onto the other side of the SSM by drop-casting with a loading mass of 2.0 mg cm<sup>-2</sup> for metal-free catalyst and 1.0 mg cm<sup>-2</sup> for Pt/C catalyst. The catalyst ink was prepared as described in the electrochemical measurements section. A polished Zn plate served as anode and the electrolyte were 6.0 M KOH for Zn-air primary batteries and 6.0 M KOH with 0.2 M Zn(Ac)<sub>2</sub> for rechargeable Zn-air batteries. The GDL has an effective area of 1 cm<sup>2</sup> and allows O<sub>2</sub> from ambient air to reach the catalyst sites.

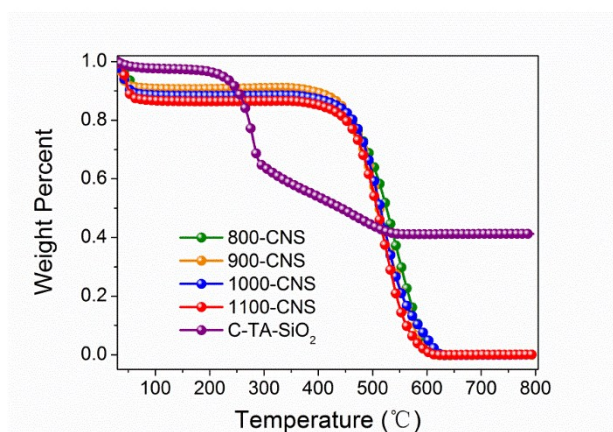


Fig. S1 Thermal gravimetric analyses of the N, S co-doped carbon samples calcined at different temperatures as well as the un-calcined pristine precursor mixture (marked as C-TA-SiO<sub>2</sub>) in O<sub>2</sub> flow. Ramp rate, 5 °C/min; O<sub>2</sub> flow, 40 mL/min.

Note: In the C-TA-SiO<sub>2</sub> mixture, the sharp weight loss starts around 220 °C is probably from the oxidation of the TA molecules, while a further gradual weight loss initiates from ca. 290 °C stems from the oxidation of the partially polymerized sucrose precursors.<sup>1</sup> The residual particles are the introduced SiO<sub>2</sub> template, which has a weight percent of 42%. When excess Teflon powder was mixed with the C-TA-SiO<sub>2</sub> mixture, the SiO<sub>2</sub> can be etched in-situ upon the pyrolysis under inert atmosphere. As shown in Fig. S1, all the pyrolyzed samples present complete weight loss in oxygen flow above 600 °C, indicating the total removal of SiO<sub>2</sub> template. To check the possible residual Si and F impurities within the pyrolyzed carbon samples, we further conducted XPS element analyses. As shown in Fig. S2, both the Si and F contents are extremely low, owing reasonably to the fact that the gaseous SiF<sub>4</sub> species from the etching reaction can be carried away by the carrier gas,<sup>1,2</sup> which also confirms the effectiveness of our synthetic approach.

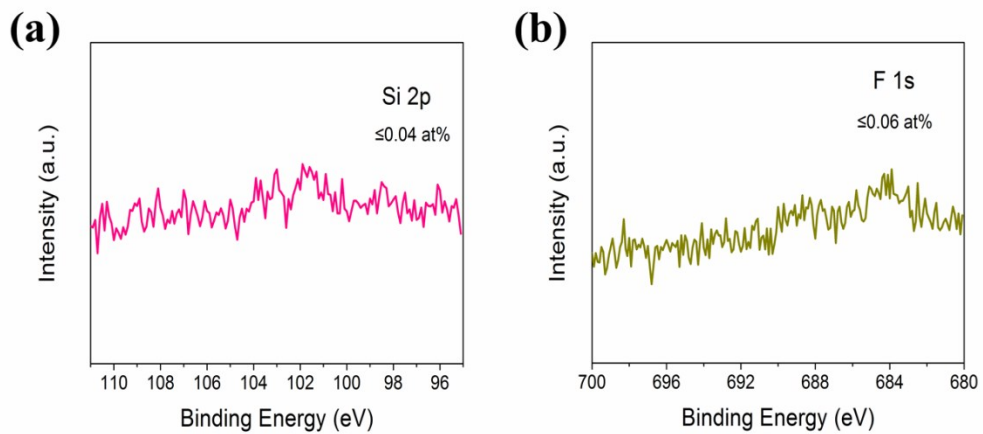


Fig. S2 High-resolution XPS spectra of the (a) Si 2p (b) F 1s core level.

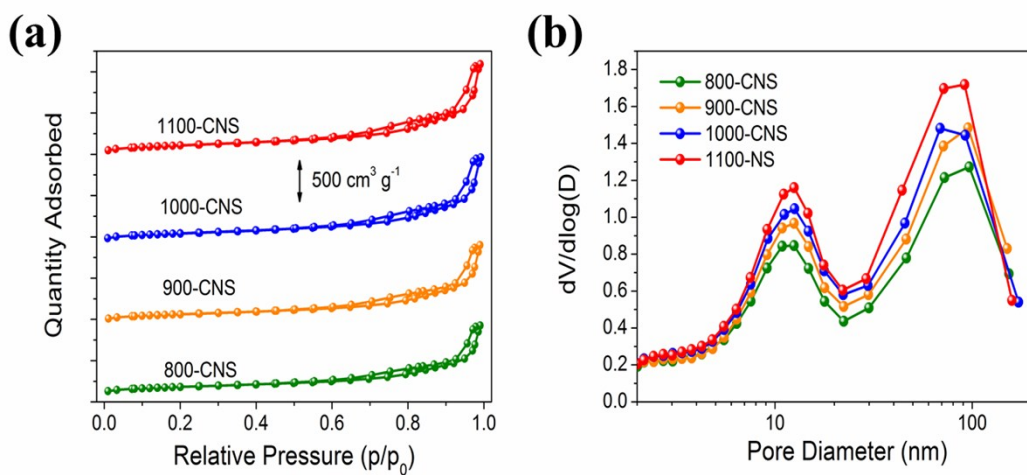


Fig. S3 (a)  $N_2$  adsorption/desorption isotherms of different samples; (b) Pore diameter distribution of all samples.

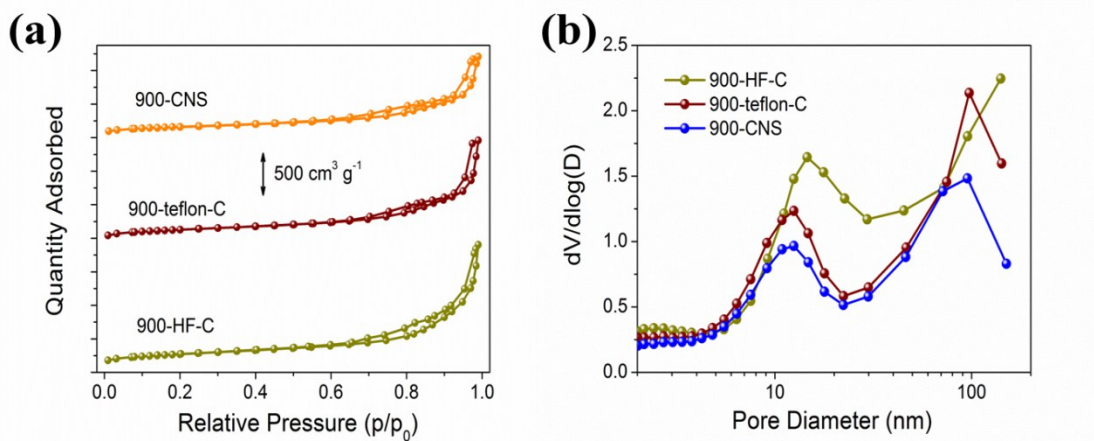


Fig. S4 (a)  $N_2$  adsorption/desorption isotherms and (b) pore size distribution plots of 900-CNS sample, one-pot etched porous carbon (900-teflon-C) and conventional two-step etched carbon (900-HF-C). A moderate temperature (900 °C) was selected to avoid the possible peculiar deviation of the parameters at higher calcination temperatures.

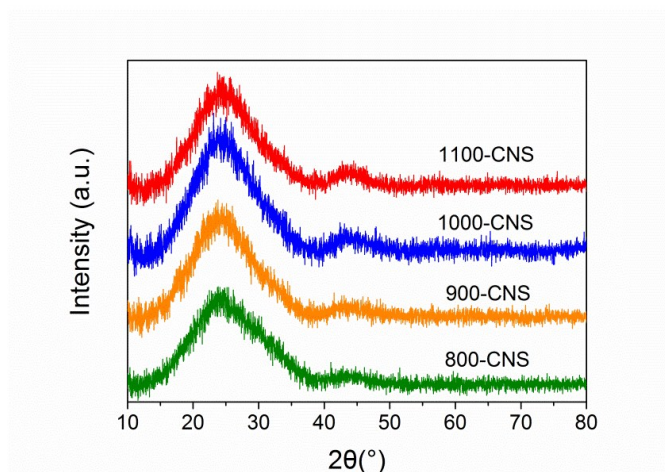


Fig. S5 XRD patterns of the N, S-enriched carbon calcined at different temperatures.

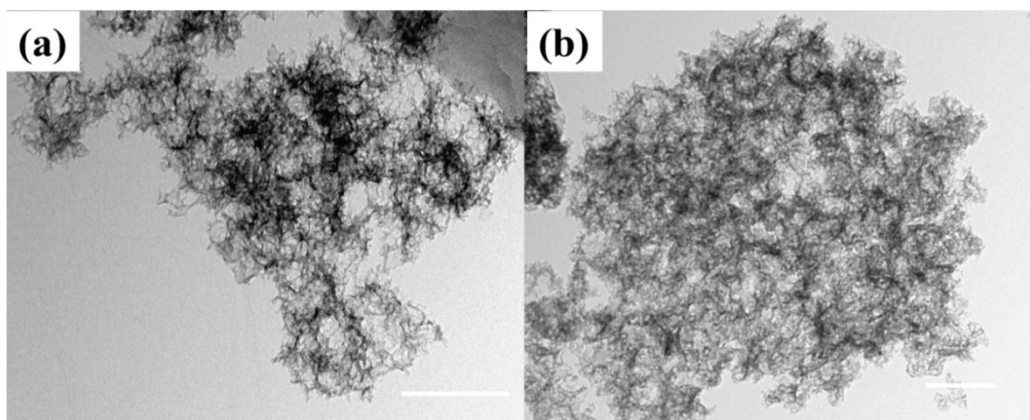


Fig. S6 TEM observation of (a) porous carbon etched by HF and (b) 1100-CNS resulted from in-situ Teflon etching.

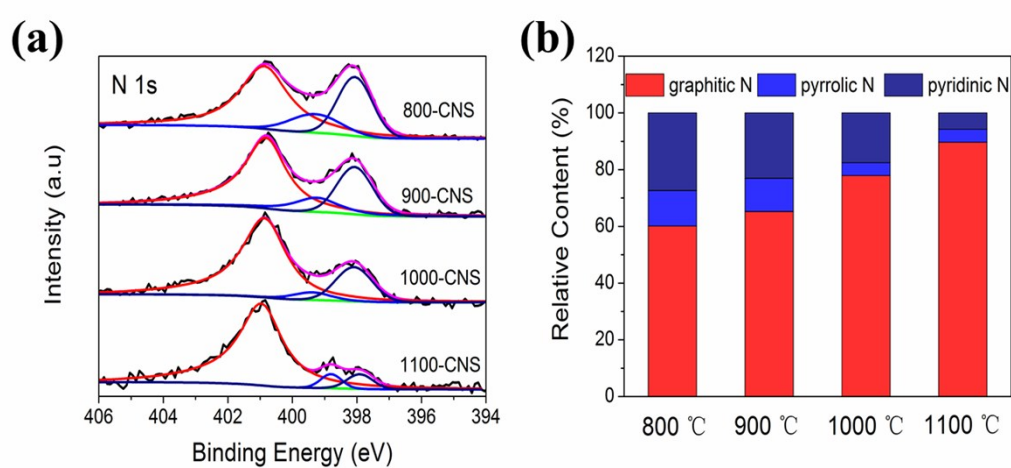


Fig. S7 (a) High resolution N 1s XPS spectra of the samples pyrolyzed at different temperatures; (b) Relative content ratios of graphitic, pyrrolic and pyridinic N species within different samples.

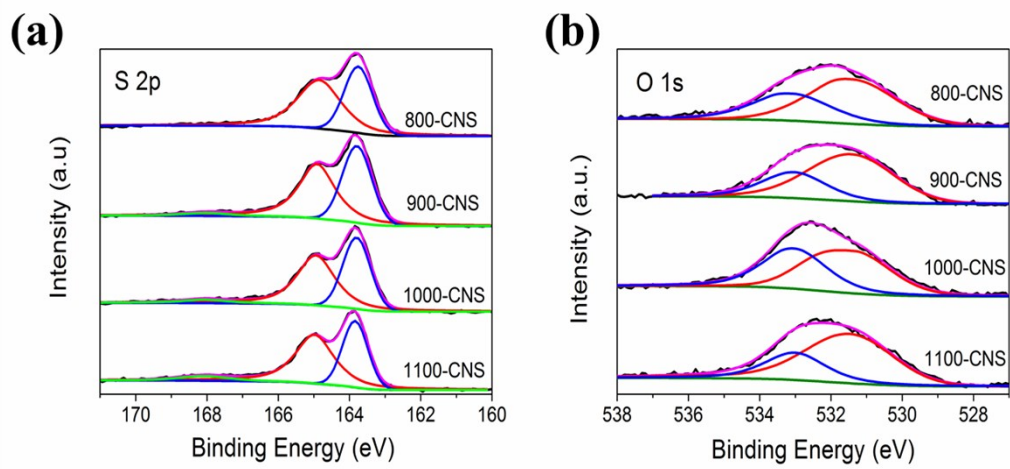


Fig. S8 High resolution (a) S 2p and (b) O1s XPS spectra of the samples.



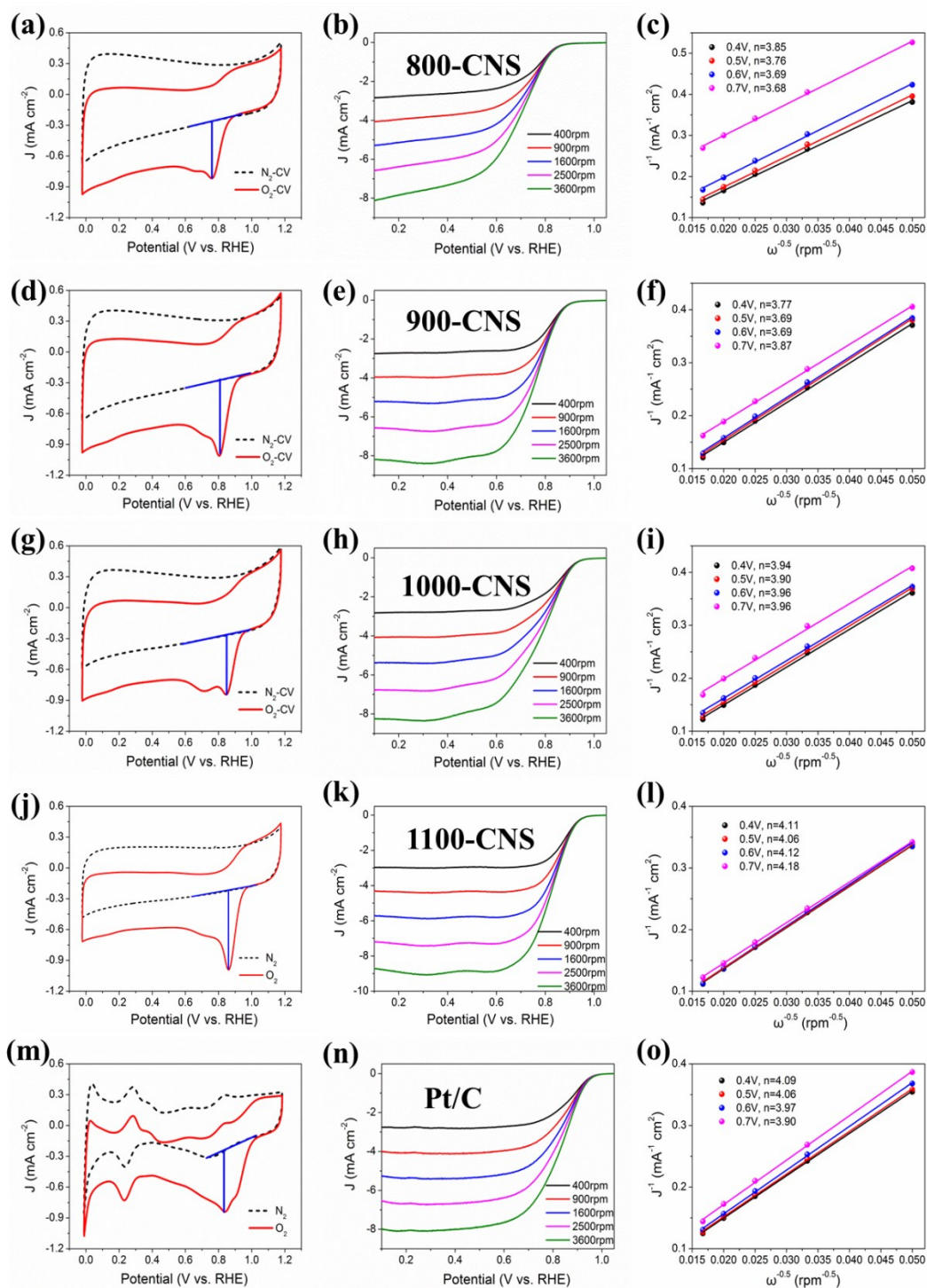


Fig. S9 (a, d, g, j, m) CV curves of different catalysts recorded at 20 mV s<sup>-1</sup> in N<sub>2</sub> and O<sub>2</sub> saturated 0.1 M KOH solution; (b, e, h, k, n) LSV curves of the catalysts at different rotation speeds; (c, f, i, l, o) K-L plots of different samples at various potentials including the corresponding electron transfer number.

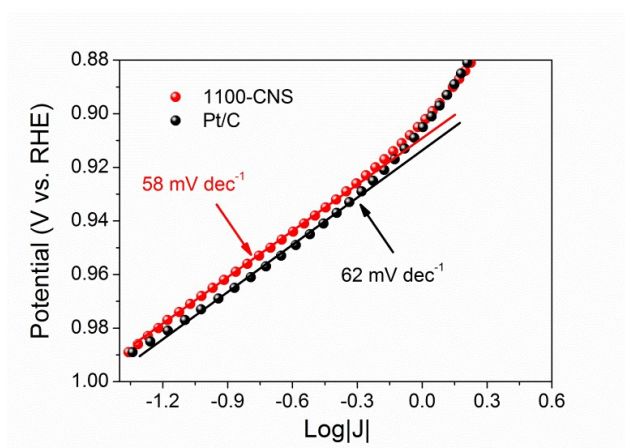


Fig. S10 Tafel plots of the 1100-CNS and Pt/C catalysts in 0.1 M KOH at 1600 rpm.

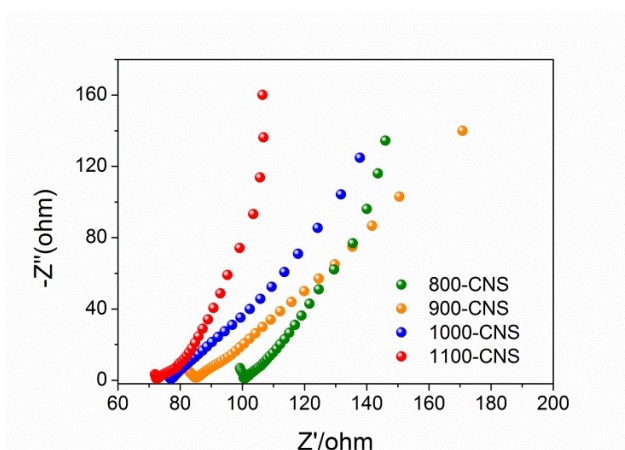


Fig. S11 Electrochemical impedance spectra of different catalysts in alkaline solution at 1600 rpm and 0.7 V (vs. RHE).

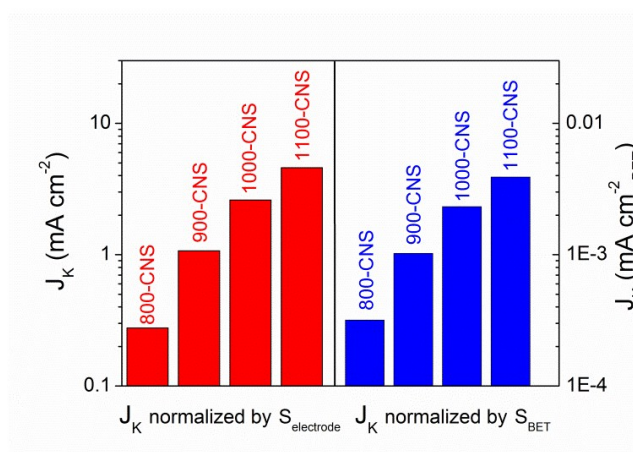


Fig. S12 Comparison of kinetic limiting currents ( $J_K$ s) of different samples obtained within the mixed kinetic-diffusion region (0.85 V vs. RHE) upon normalization of the electrode area and the BET surface area.

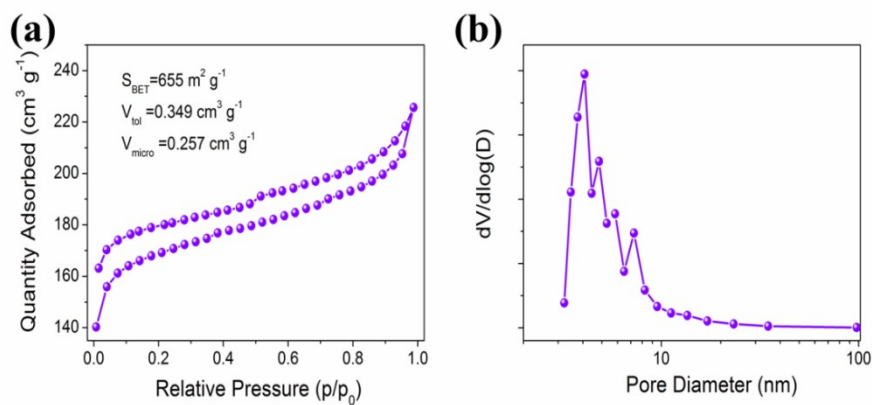


Fig. S13 (a) N<sub>2</sub> adsorption/desorption isotherms and (b) pore diameter distribution of the template-free (1100-CNS-SiO<sub>2</sub> free) sample. The micropore volume was determined by the t-plot analysis.

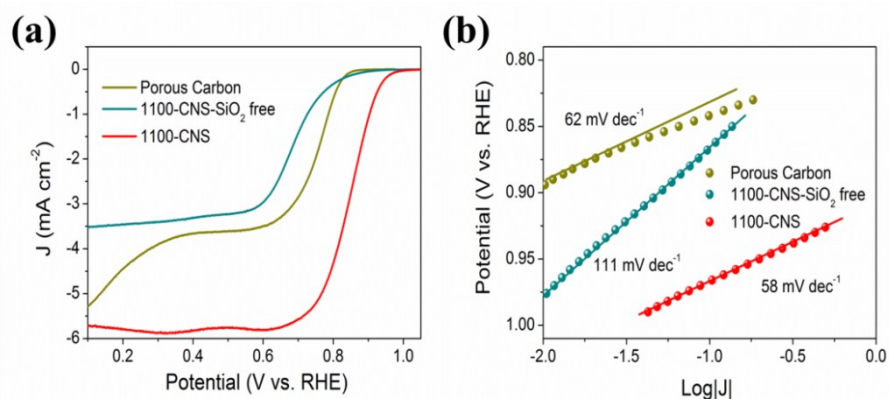


Fig. S14 (a) LSV curves of the 1100-CNS sample as well as the controlled bare porous carbon (dopant-free) and 1100-CNS-SiO<sub>2</sub> free (template-free) samples at 1600 rpm in 0.1 M KOH; (b) The corresponding Tafel plots including the Tafel slopes.

Note: The dopant-free sample features a similar Tafel slope compared with the 1100-CNS sample, suggesting a similar mass transport resistance; however, the ORR onset potential of this bare carbon sample is obviously smaller than the 1100-CNS one, denoting an inferior activity. The template-free sample, conversely, gives a comparable onset potential but with remarkably larger Tafel slope, indicating the oxygen transport is hindered by the absence of macropores.<sup>3</sup> Similar results were also evinced by the CV tests and RDE tests at different rotation speeds in Fig. S15. The half-wave potential ( $E_{1/2}$ ) of the 1100-CNS-SiO<sub>2</sub> free sample is the smallest among the three samples, whilst the apparent plateau in the LSV curves of the bare carbon sample indicates an inefficient oxygen reduction process via a two-electron ( $2e^-$ ) reaction path.<sup>3-5</sup> These results therefore validate that both the macropore and the dopant species play crucial role in the prominent ORR activity of the 1100-CNS sample.

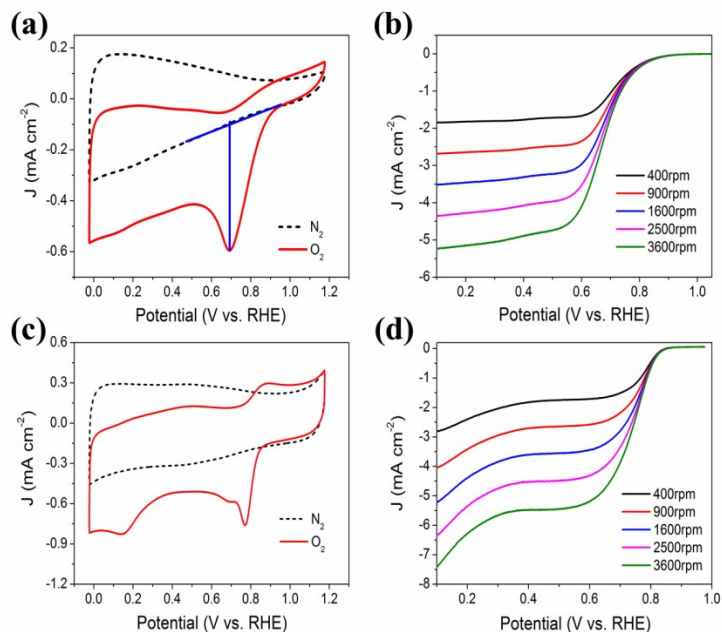


Fig. S15 Electrochemical catalytic performance toward ORR in 0.1 M KOH solution of the control samples: CV scans of the (a) template-free pyrolyzed (1100-CNS-SiO<sub>2</sub> free) sample and (c) bare porous carbon (dopant-free) substrate; LSV curves of the (b) 1100-CNS-SiO<sub>2</sub> free and (d) bare carbon samples at different rotating speeds.

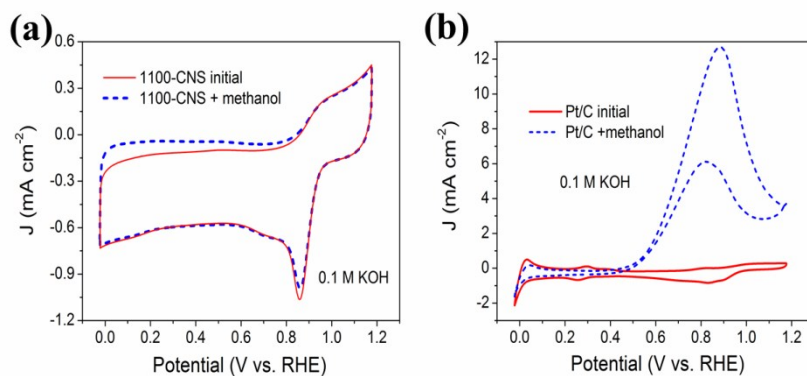


Fig. S16 Cross-over tolerance tests of the representative (a) 1100-CNS and (b) Pt/C samples before and after the addition of 10 vol% methanol into 0.1 M KOH. The drastic anodic current of the Pt/C modified electrode resulted from significant methanol oxidation reaction, suggesting the susceptible selectivity of Pt/C catalyst.

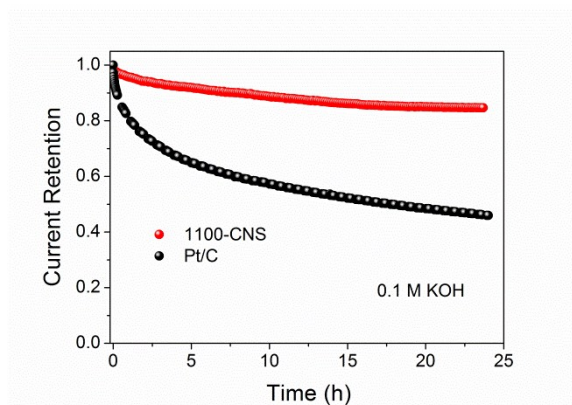


Fig. S17 Chronoamperometric durability tests of the 1100-CNS and referenced Pt/C samples at 1600 rpm and 0.7 V (vs. RHE) in  $O_2$  saturated 0.1 M KOH.

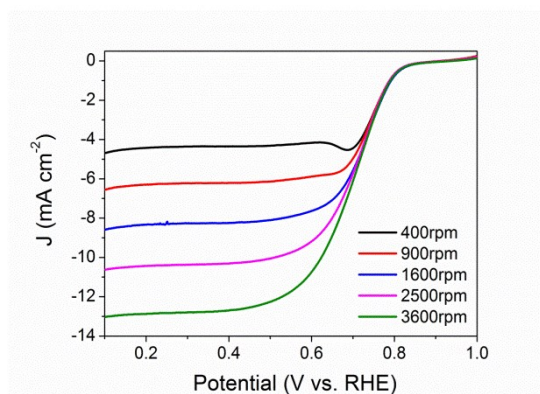


Fig. S18 LSV curves of the 1100-CNS sample in 0.1 M  $HClO_4$  at different rotation speeds.

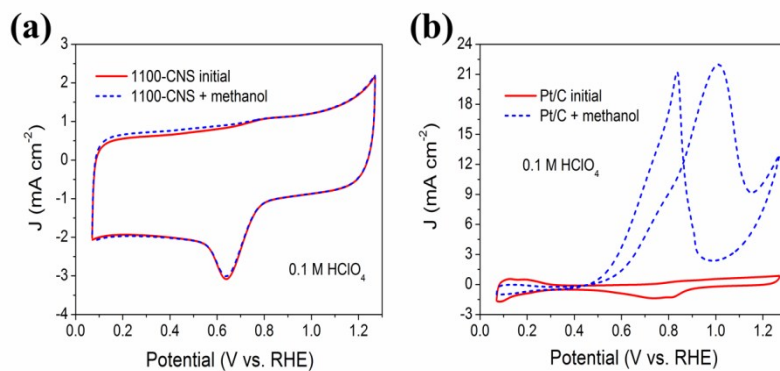


Fig. S19 Cross-over tolerance tests of the representative (a) 1100-CNS and (b) Pt/C samples before and after the addition of 10 vol% methanol into 0.1 M  $HClO_4$ .

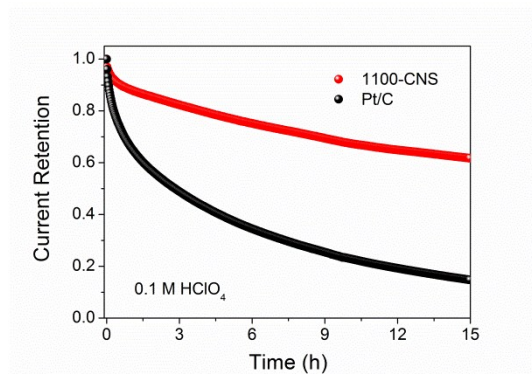


Fig. S20 Chronoamperometric durability tests of the 1100-CNS and referenced Pt/C samples at 1600 rpm and 0.7 V (vs. RHE) in O<sub>2</sub> saturated 0.1 M HClO<sub>4</sub>.

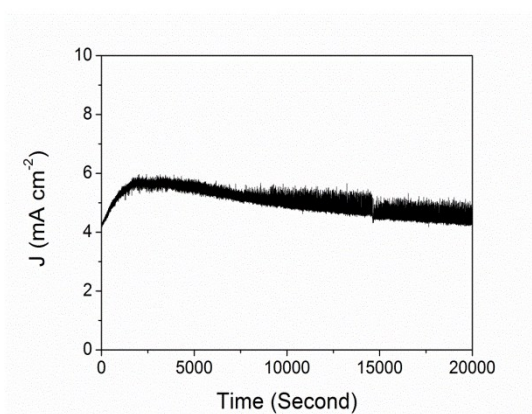


Fig. S21 Chronoamperometric durability test of the 1100-CNS at 1.60 V (vs. RHE) in 0.1 M KOH, iR not corrected.

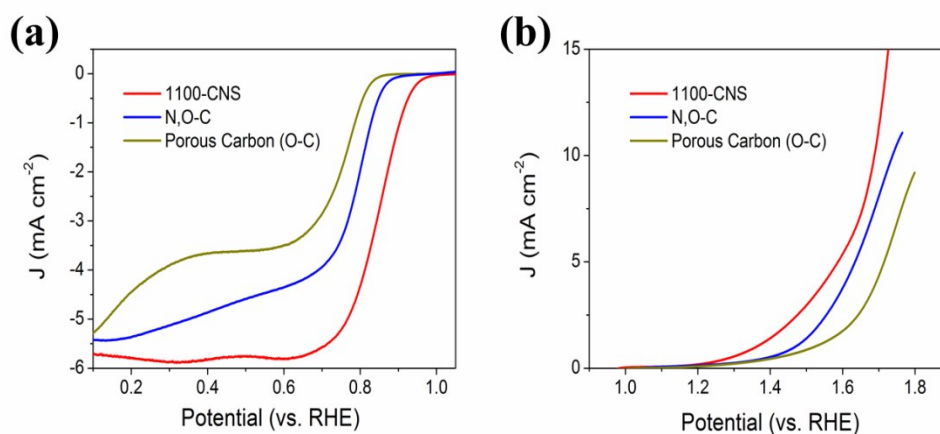


Fig. S22 LSV curves of different samples for (a) ORR and (b) OER at 1600 rpm in 0.1 M KOH. The 1100-CNS sample is enriched with N, S as well as residual O heteroatoms. The controlled N, O co-doped sample (N, O-C) was synthesized with identical procedure for that of the 1100-CNS one except for replacing trithiocyanuric acid ( $C_3H_3N_3S_3$ ) with melamine ( $C_3H_6N_6$ ). Bare porous carbon (O-C) was also measured to review the role of residual oxygen element.

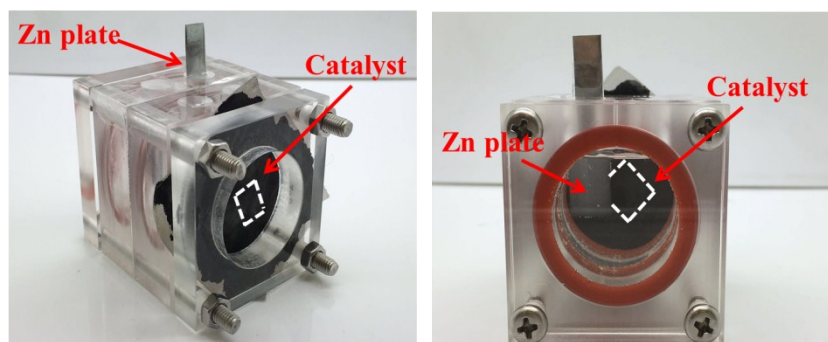


Fig. S23 Side-view and front-view of the static Zn-air battery device. The shown Zn plate is  $1 \times 1.5$  cm in size while all casted catalysts are  $1 \times 1$  cm in size.



Table 1 Porous structural characteristics and elemental compositions of different samples

Sample	S <sub>BET</sub>	S <sub>micro</sub>	V <sub>tol</sub>	V <sub>micro</sub>	Element Ratio (wt%)				
	m <sup>2</sup> g <sup>-1</sup>		cm <sup>3</sup> g <sup>-1</sup>		C	O	N	S	N+S
800-CNS	624	220	1.403	0.106	87.59	2.78	4.83	4.8	9.63
900-CNS	749	321	1.606	0.157	89.38	2.9	3.3	4.41	7.71
1000-CNS	801	347	1.762	0.169	90.29	3.5	2.59	3.62	6.21
1100-CNS	840	364	1.877	0.177	93.64	3.15	1.33	1.88	3.21
900-teflon-C	849	335	1.995	0.163	96.38	3.62	-	-	-
900-HF-C	763	169	2.316	0.079	95.86	4.14	-	-	-
900-HF-CNS	528	45	2.186	0.017	90.19	3.42	3.09	3.30	6.39

Note: the two-step synthesized samples are marked as 900-HF-XX (C for bare carbon, CNS for N, S-enriched carbon); 900-teflon-C is the one-pot pyrolyzed bare carbon material.

Table S2 Comparison study of some advanced metal-free ORR catalysts in 0.1 M KOH electrolyte

Catalyst	Loading Mass (mg cm <sup>-2</sup> )	Onset Potential (V vs. RHE)	Half-wave Potential (V vs. RHE)	Limiting-Current Density @1600 rpm (mA cm <sup>-2</sup> )	Reference
N-doped carbon nanotube arrays	-	0.97	0.84	5.6	Science <b>2009</b> , 323, 760
C <sub>3</sub> N <sub>4</sub> @mesoporous carbon	0.28	0.87	0.75	3.7	J. Am. Chem. Soc. <b>2011</b> , 133, 20116
N-graphene QDs	0.28	0.76	0.65	2.7	J. Am. Chem. Soc. <b>2012</b> , 134, 15
B, N-graphene	0.28	0.86	0.68	5.2	Angew. Chem. Int. Ed. <b>2013</b> , 52, 3110
Te, P-doped porous carbon fiber	0.1	0.89	0.79	5.7	J. Am. Chem. Soc. <b>2014</b> , 136, 14385
N-doped meso/micro porous carbon	0.1 (0.5)	0.92 (0.92)	0.85 (0.87)	5.8 (5.8)	Nature Commun. <b>2014</b> , 5, 4973
N, S-doped graphene	0.35	0.87	0.61	1.8	Adv. Mater. <b>2014</b> , 26, 6186
N, P-doped mesoporous carbon	0.15	0.94	0.85	4.3	Nature Nanotech. <b>2015</b> , 10, 444
N-doped hierarchical porous carbon	0.29	-	0.85	5.4	ACS Nano <b>2016</b> , 10, 4364
N-doped porous carbon	0.29	0.98	0.88	5.5	Adv. Energy Mater. <b>2016</b> , 1502389
N-doped porous carbon nanosheets	0.2	0.9	0.77	5.79	Adv. Mater. <b>2016</b> , 28, 5080
N, S-doped carbon nanosheets	0.2	0.92	0.77	4.3	Nano Energy <b>2016</b> , 19, 373
N-doped porous carbon fiber	0.1	0.97	0.82	4.7	Adv. Mater. <b>2016</b> , 28, 3000
N, P-doped CGHNs	0.3	0.94	0.82	5.6	Adv. Mater. <b>2016</b> , 28, 4606
N-doped graphene	0.6	0.92	0.84	5.5	Sci. Adv. <b>2016</b> , 2:e1501122
N, S-doped porous carbon	0.14 (0.42)	0.99 (0.99)	0.85 (0.88)	5.8 (6.4)	This work

Table S3 Comparison study of some advanced metal-free and non-noble metal based ORR catalysts in acidic electrolyte

Catalyst	Loading Mass (mg cm <sup>-2</sup> )	Onset Potential (V vs. RHE)	Half-wave Potential (V vs. RHE)	Limiting-Current Density @1600 rpm (mA cm <sup>-2</sup> )	Electrolyte	Reference
N-doped mesoporous carbon	0.8	0.8	0.5	4.5	0.1 M HClO <sub>4</sub>	J. Am. Chem. Soc. <b>2011</b> , 133, 206
N-carbon spheres	0.25	0.65	0.42	5.5	0.5 M H <sub>2</sub> SO <sub>4</sub>	Adv. Mater. <b>2013</b> , 25, 998
N-doped meso/microporous carbon	0.5	0.84	0.72	4.6	0.5 M H <sub>2</sub> SO <sub>4</sub>	Nature Commun. <b>2014</b> , 5, 4973
N-doped mesoporous carbon sheet	0.6	0.75	0.57	5	0.5 M H <sub>2</sub> SO <sub>4</sub>	Angew. Chem. Int. Ed. <b>2014</b> , 53, 1570
N, P-doped mesoporous carbon	0.45	0.82	0.62	5.6	0.1 M HClO <sub>4</sub>	Nature Nanotech. <b>2015</b> , 10, 444
N, P-doped CGHNs	0.6	0.9	0.68	5.7	0.1 M HClO <sub>4</sub>	Adv. Mater. <b>2016</b> , 28, 4606
Fe-N-C	0.1	0.82	0.6	6	0.1 M HClO <sub>4</sub>	J. Am. Chem. Soc. <b>2014</b> , 136, 11027
Fe <sub>3</sub> C-C	0.6	0.9	0.73	5.5	0.1 M HClO <sub>4</sub>	Angew. Chem. Int. Ed. <b>2014</b> , 53, 3675
Fe <sub>3</sub> C-CNT	1.2	0.89	0.63	ca. 6	0.5 M H <sub>2</sub> SO <sub>4</sub>	J. Am. Chem. Soc. <b>2015</b> , 137, 1436
Fe-N-C nanofiber	0.6	0.84	0.62	5	0.5 M H <sub>2</sub> SO <sub>4</sub>	Angew. Chem. Int. Ed. <b>2015</b> , 54, 8179
N, S-doped porous carbon	0.6 (0.6)	0.88 (0.88)	0.73 (0.72)	8.3 (8.2)	0.1 M HClO <sub>4</sub> (0.5 M H <sub>2</sub> SO <sub>4</sub> )	This work

Table S4 Comparison study of some recently reported bi-functional ORR/OER catalysts in alkaline electrolyte

Catalyst	Loading Mass (mg cm <sup>-2</sup> )	OER Onset Potential (V vs. RHE)	OER E <sub>J=10</sub> (V vs. RHE)	ORR E <sub>1/2</sub> (V vs. RHE)	ΔE (E <sub>J=10</sub> - E <sub>1/2</sub> ) (V)	Electrolyte	Reference
MnO <sub>x</sub> Film	-	1.30	1.77	0.73	1.04	0.1 M KOH	J. Am. Chem. Soc. <b>2010</b> , 132, 13612
Co <sub>3</sub> O <sub>4</sub> /N-doped graphene	1.0	1.40	1.54	0.83	0.71	1 M KOH	Nat. Mater. <b>2011</b> , 10, 780
H-Pt/CaMnO <sub>3</sub>	0.085	1.50	1.80	0.79	1.01	0.1 M KOH	Adv. Mater. <b>2014</b> , 26, 2047
Mn <sub>x</sub> O <sub>y</sub> /N-doped carbon	0.21	1.55	1.68	0.81	0.87	0.1 M KOH	Angew. Chem. Int. Ed. <b>2014</b> , 53, 8508
CoO/N-doped graphene	0.7	1.30	1.57	0.81	0.76	1 M KOH	Energy Environ. Sci. <b>2014</b> , 7, 609
Fe@N-C	0.31	ca. 1.52	1.71	0.83	0.88	0.1 M KOH	Nano Energy <b>2015</b> , 13, 387
P-doped C <sub>3</sub> N <sub>4</sub> on carbon-fiber paper	0.2	1.53	1.63	0.67	0.96	0.1 M KOH	Angew. Chem. Int. Ed. <b>2015</b> , 54, 4646
N-doped porous carbon fiber	0.1	1.43	1.84	0.82	1.02	0.1 M KOH	Adv. Mater. <b>2016</b> , 28, 3000
N, S-doped carbon nanosheet	0.2	-	1.65	0.77	0.88	0.1 M KOH	Nano Energy <b>2016</b> , 19, 373
N-doped graphene	0.3	1.53 (1.51)	1.66 (1.59)	0.84 (0.84)	0.82 (0.75)	0.1 M KOH (1 M KOH)	Sci. Adv. <b>2016</b> , 2:e1501122
N, S-doped porous carbon	0.42	1.30 (1.30)	1.69 (1.60)	0.88 (0.88)	0.81 (0.72)	0.1 M KOH (1 M KOH)	This Work

### References

- S1. D. K. Singh, K. S. Krishna, S. Harish, S. Sampath and M. Eswaramoorthy, *Angew. Chem. Int. Ed.*, 2016, **55**, 2032.
- S2. J. Conesa and R. Font, *Polym. Eng. Sci.*, 2001, **41**, 2137.
- S3. J. Liang, Y. Zheng, J. Chen, J. Liu, D. Hulicova - Jurcakova, M. Jaroniec and S. Z. Qiao, *Angew. Chem. Int. Ed.*, 2012, **51**, 3892.
- S4. J. Liang, Y. Jiao, M. Jaroniec and S. Z. Qiao, *Angew. Chem. Int. Ed.*, 2012, **51**, 11496.
- S5. Z. Pei, J. Zhao, Y. Huang, Y. Huang, M. Zhu, Z. Wang, Z. Chen and C. Zhi, *J. Mater. Chem. A*, 2016, **4**, 12205.